



Nanoscale

**Kinetically assembled binary nanoparticle networks**

Journal:	<i>Nanoscale</i>
Manuscript ID	NR-ART-11-2019-009900.R1
Article Type:	Paper
Date Submitted by the Author:	26-Jan-2020
Complete List of Authors:	Wang, Jiuling; Duke University, Mechanical Engineering & Materials Science Lee, Brian; Duke University, Mechanical Engineering and Materials Science Arya, Gaurav; Duke University, Mechanical Engineering & Materials Science; Duke University

SCHOLARONE™  
Manuscripts

Cite this: DOI: 00.0000/xxxxxxxxxx

# Kinetically assembled binary nanoparticle networks<sup>†</sup>

Jiuling Wang,<sup>a</sup> Brian Hyun-jong Lee,<sup>a</sup> and Gaurav Arya<sup>\*a</sup>

Received Date

Accepted Date

DOI: 00.0000/xxxxxxxxxx

Embedding percolating networks of nanoparticles (NPs) within polymers is a promising approach for mechanically reinforcing polymers and for introducing novel electronic, transport, and catalytic properties into otherwise inert polymers. While such networks may be obtained through kinetic assembly of unary system of NPs, the ensuing structures exhibit limited morphologies. Here, we investigate the possibility of increasing the diversity of NP networks through kinetic assembly of multiple species of NPs. Using lattice Monte Carlo simulations we show that networks obtained from co-assembly of two NP species of different sizes exhibit significantly more diverse morphology than those assembled from a single species. In particular, we achieved considerable variations in the particle spatial distribution, proportions of intra- and interspecies contacts, fractal dimension, and pore sizes of the networks by simply modulating the stoichiometry of the two species and their intra and inter-species affinities. We classified these distinct morphologies into “integrated”, “coated”, “leaved”, and “blocked” phases, and provided relevant phase diagrams for achieving them. Our findings are relevant to controlled and predictable assembly of particle networks for creating multifunctional composites with improved properties.

## 1 Introduction

Nanoparticles (NPs) are often added to polymers to improve their mechanical properties or introduce new functions into the polymers.<sup>1,2</sup> The spatial distribution of NPs plays a critical role in governing the properties of the resulting polymer nanocomposites. In general, NPs can be present in *three* distinct states: dispersed, ordered, or random aggregate. In the *dispersed* state, the NPs remain stably separated from each other due to repulsive or weak interparticle interactions. This state represents the most common scenario in applications, as it provides spatially uniform and predictable enhancement in properties, usually proportional to the NP loading fraction.<sup>3,4</sup> In the *ordered* state, the NPs exhibit stronger interactions and self-assemble into strings, sheets, or globular superstructures with periodic arrangement of particles.<sup>5–8</sup> This requires the particles to be highly uniform in size and shape, and also demands stringent thermodynamic assembly conditions for the NPs to attain their globally stable configuration, both of which are challenging to achieve in the case of nanoscopic particles in viscous polymer melts. The more likely outcome of NP assembly within polymers is the *random aggregate* state, where NPs get kinetically trapped into fractal, often

percolating networks.<sup>9,10</sup> Such random fractal and percolating structures have many promising applications. For example, percolating NP structures provide significantly higher mechanical reinforcement to polymers in the melt state than dispersed NPs at equivalent loadings.<sup>5,11</sup> Fractal and percolating NP structures embedded within a polymer could also find applications in solid-state electrolytes,<sup>12,13</sup> flame retardants,<sup>14</sup> and in catalysis and sensing.<sup>15,16</sup>

Kinetically-trapped aggregates of particles are ubiquitous in nature, occurring in systems as diverse as colloids,<sup>17,18</sup> aerosols,<sup>19</sup> foods,<sup>20</sup> soot,<sup>21</sup> and blood clots.<sup>22</sup> The mechanism and kinetics of aggregation, and the morphology of the resulting aggregates, are well described by the cluster-cluster aggregation (CCA) model.<sup>23,24</sup> In this model, diffusing particles stick to each other irreversibly upon contact to form rigid clusters, which continue to diffuse and grow by colliding with other diffusing particles or clusters. A cluster size-dependent diffusivity is often considered and so is a contact area-dependent sticking probability which accounts for the presence of energy barriers in the interparticle interaction potential that may prevent particles from sticking the instant they come into close proximity.<sup>25–28</sup> Depending on the relative timescales of diffusion *versus* sticking, two regimes emerge: diffusion-limited cluster aggregation (DLCA) and reaction-limited cluster aggregation (RLCA).<sup>17</sup> In the DLCA regime, the energy barrier is negligible, so the aggregation kinetics are limited by the collision time of particles, and the assembled structures are more tenuous and extended.<sup>23,24</sup> In contrast, in the RLCA regime, the

<sup>a</sup> Department of Mechanical Engineering and Materials Science, Duke University, Durham, North Carolina 27708, United States. Fax: 919-660-8963; Tel: 919-660-5435; E-mail: gaurav.arya@duke.edu

<sup>†</sup> Electronic Supplementary Information (ESI) available. See DOI: 00.0000/00000000.

aggregation kinetics are limited by the time taken by the particles to overcome the repulsive barrier, and the formed structures are denser with a higher fractal dimension.<sup>29</sup>

Most aggregation studies have focused on systems containing a *single* species of particles. According to the CCA model, the size distribution and morphology of aggregates in monodisperse systems is controlled by particle volume fraction, their sticking probability, and the scaling of diffusivity with respect to cluster size,<sup>23,24,29</sup> though this last parameter is usually constrained by physical laws such as the Stokes-Einstein relationship where diffusivity scales inversely with cluster dimension. While extreme values of the above parameters can lead to low- and high-density aggregates characteristic of the DLCA and RLCA regimes, the overall morphology remains random fractal-like. Furthermore, as we recently showed,<sup>25,30</sup> NPs aggregating within polymer thin films exhibit striking similarity in cluster growth and morphology, irrespective of the particle size and shape and the molecular weight of the polymer matrix. For instance, in all studied systems, the mean size of NP clusters grew as a power-law with time and their size distributions at all time points (except early stages of assembly) exhibited characteristic bell-shaped curves that could be collapsed onto a universal “master curve” upon appropriate time and size normalization based on CCA theory.<sup>25</sup> Thus, achieving unique and complex aggregate morphologies seems to be beyond the reach of monodisperse systems.

In this work, we explore the possibility of expanding the diversity of NP assembly morphologies achievable by random aggregation through the introduction of a *second* species of NPs of size, diffusivity, and sticking propensity different from the first species. We hypothesize that the addition of a new, distinct NP species will introduce additional length and time scales into the assembly system and alter the sequence of assembly events, leading to new and interesting aggregate morphologies. For instance, depending on the affinity between the two species, the larger, slow-diffusing NPs could act as obstacles or seeds to the assembly of the smaller, more mobile NPs.<sup>31–35</sup> Indeed, a few studies have shown the potential of co-assembly of binary NPs in creating mesoscale-sized structures and interpenetrating gels.<sup>10,36,37</sup> To investigate such kinetic co-assembly of two species of NPs, we used lattice-based CCA simulations, an approach that allowed us to efficiently capture differences in the size, diffusivities, and contact areas of the two species of NPs, as well as differences in affinities within and across species, permitting rapid exploration of the vast parameter space. We demonstrate that the time scale of intra- versus inter-species assembly events can be tuned by the affinities between NPs and exploited to create a variety of heterogeneous structures, which we classify as “integrated”, “coated”, “leaved” and “blocked” phases. We characterize the local spatial organization, composition, porosity, fractal dimension, and structural factor of these structures. Such structures with unique and controllable spatial distribution of NPs could lead to polymer nanocomposites with novel mechanical,<sup>3,4</sup> electromagnetic,<sup>38,39</sup> and optical properties.<sup>16,40</sup>

## 2 CCA Simulations

As a first step to exploring the full range of aggregate morphologies achievable through kinetic assembly of heterogeneous systems of NPs, we considered a binary system of large and small NPs and studied their co-assembly using the CCA model simulated on a two-dimensional (2D) lattice. As shown previously,<sup>30</sup> this model captures well the most salient aspects of NP aggregation in polymers while enabling efficient exploration of the parameter space. The 2D geometry not only allows for easy visualization of NP aggregates and computational efficiency, but also represents the common experimental scenario of NPs aggregating at fluid-fluid interfaces<sup>41</sup> or within polymer thin films.<sup>7,30</sup>

All CCA simulations were conducted on a  $400 \times 400$  square lattice and implemented periodic boundary conditions to avoid boundary effects. Each of the small and large NPs denoted by “NP1” and “NP2” occupied  $1 \times 1$  and  $4 \times 4$  lattice sites, respectively (Fig. S1). This size ratio implies that the diffusivity of NP2 is about one-seventh of that of NP1 (based on the Stokes-Einstein relationship discussed below) and the surface area is four times larger. We performed simulations with varying numbers  $N_1$  and  $N_2$  of the two species to explore the effects of *particle area density*  $\rho$  (fraction of lattice sites occupied by NPs) and *species area fractions*  $\phi_1$  or  $\phi_2 = 1 - \phi_1$  (fraction of particle-occupied sites occupied by NP1 or NP2). In particular, we considered  $N_1$  in the range 10,000 to 30,000 and  $N_2$  in the range 200 to 800 (all parameters used in this study are summarized in Table 1), yielding particle area densities in the range  $\rho = 0.0825$  to  $0.2675$  and NP2 area fractions in the range  $\phi_2 = 0.10$  to  $0.56$ . We also explored the effects of varying probabilities  $p_{11}$ ,  $p_{12}$  and  $p_{22}$  for individual NPs to stick together when they collide with each other. These probabilities were varied between  $10^{-4}$  to  $0.4$ , reflecting different modifications of the NP surfaces that lead to distinct association energy barriers. Consistent with previous analysis of the aggregation dynamics of polymer-grafted NPs,<sup>25</sup> we chose a maximum sticking probability of  $0.4$  to reflect the presence of a small energy barrier that prevents instantaneous bonding of NPs. We considered irreversible sticking of particles, a situation prevalent across many particle systems<sup>10,42,43</sup> that arises from strong interparticle interactions, which lead to large energy barriers for cluster dissociation.<sup>28</sup> The above prescription allowed us to introduce distinct diffusivities, NP stoichiometries, and assembly affinities between NPs into the system.

Each simulation was initiated by randomly placing onto the lattice the desired amounts of the two species, ensuring that no two NPs occupy the same lattice site. For convenience we will use the

**Table 1** Parameters values used in CCA simulations

Parameter	Value
$p_{11}$	$10^{-4}$ , $10^{-2}$ , $0.4$
$p_{12}$	$10^{-4}$ , $10^{-2}$ , $0.4$
$p_{22}$	$10^{-4}$ , $10^{-2}$ , $0.4$
$\gamma$	$-0.7$
$N_1$	10 000, 20 000, 30 000
$N_2$	200, 400, 800

term “cluster” to denote both isolated NPs and their growing clusters. The diffusion of clusters was modeled as a random walk on the lattice with self-diffusivity  $D_s$  given by

$$D_s = D_0 (s/s_0)^\gamma \quad (1)$$

where  $s$  is the size of the cluster measured in terms of the number of lattice sites it occupies,  $s_0 = 1$  and  $D_0$  are the size and self-diffusivity of a reference cluster occupying a single lattice site, i.e., an isolated NP1, and  $\gamma$  is a scaling coefficient that reflects the size-dependence of the diffusivity of clusters.<sup>25</sup> According to Stokes-Einstein relationship, the diffusivity decays as  $D_s \sim R_h^{-1}$  with the hydrodynamics radius  $R_h$  of the cluster. For nonspherical clusters,  $R_h$  is usually assumed to be equal to the radius of gyration of the cluster  $R_g$ ,<sup>44</sup> which can then be related to the fractal dimension  $d_f$  of fractal clusters via  $R_g \sim s^{1/d_f}$ ,<sup>45</sup> yielding  $D_s \sim s^{-1/d_f}$ . Comparing with Eq. (1), we obtain  $\gamma = -1/d_f$ . Based on  $d_f \approx 1.4$  obtained from image analysis of NP aggregates formed within polymer thin films,<sup>7,30</sup> we set the value of  $\gamma$  to  $-0.7$ . Estimating cluster diffusivities via Eq. 1 thus avoids the cost of computing instantaneous values of  $R_g$  or  $d_f$  for each and every cluster at each simulation step.

At the beginning of the simulation, when isolated NP1s still exist, the time step was set at  $\Delta t = \tau$ , where  $\tau = 1$  is the unit of time in our simulations. At each time step, an attempt was made to move each and every cluster by one lattice site along a random direction with probability  $D_s/D_0 = (s/s_0)^\gamma$ . If the move resulted in an overlap between two clusters, the move was rejected, and the cluster stayed in its previous position. After all clusters had completed their attempted moves, if two NPs belonging to different clusters were in contact with each other, then these two clusters were merged together into one cluster with probability  $p_{ij}$ , which depends on the identities of the contacting NPs, i.e., NP1 or NP2. At some point during the simulation, all the isolated NP1s would get exhausted. If one continues to use  $\tau$  as the time step, the move probabilities given by  $(s/s_0)^\gamma$  would become increasingly smaller as the clusters grow, causing the simulations to become increasingly inefficient. This issue can be easily resolved by using an adaptive time step.<sup>25</sup> At each time step, we identify the smallest cluster in the system, whose size is denoted by  $s_{\min}$ , and increase the move probability of each cluster to  $D_s/D_{\max} = (s/s_{\min})^\gamma$ , where  $D_{\max}$  is the diffusivity of this smallest cluster with  $D_{\max} = D_0(s_{\min}/s_0)^\gamma$ . To compensate for this increased mobility, the time step is multiplied by this same factor, i.e,  $\Delta t = (D_0/D_{\max})\tau$ . Thus, the adaptive time step keeps the move probability of the smallest cluster to 1 without sacrificing any accuracy. The sticking protocol at the end of the moves remains the same as described above. The simulations were stopped when all NPs had assembled into a single cluster. All the results were averaged over 3 independent simulations with different initial NPs positions.

The above 2D lattice model makes several assumptions about NP assembly. First and foremost, it assumes a single co-planar system of NPs, e.g., at an interface or in a ultrathin film, and thus any interfacial deformations and wetting-dewetting effects occur-

ring in real systems are neglected. Second, the model accounts for spatially-dependent interactions between NPs only in terms of their “effects”: the overlap criterion that prevents NPs from occupying the same lattice site accounts for the sharp excluded-volume repulsion in the NP-NP interactions; the irreversible bonding of NPs assumes a deep potential well that prevents NP clusters from dissociating within aggregation timescales; and sticking probabilities smaller than unity account for association energy barriers, e.g., from polymer brushes on NPs. Third, the lattice model can only accommodate translational diffusion of clusters, and rotational effects are essentially ignored. Lastly, the model assumes the formation of rigid clusters whose branches cannot deform in response to interactions with other clusters.

## 3 Results

### 3.1 Overall morphology

We first examined the overall structure of the formed NP aggregates, specifically how their morphology varied with the various parameters of the system. We focused on the effects of varying the sticking propensity of NPs, that is, the sticking probabilities  $p_{11}$ ,  $p_{12}$ , and  $p_{22}$  associated with the three kinds of NP-NP contacts. Varying the numbers  $N_1$  and  $N_2$  produced more subtle effects that are discussed later in Sec. 3.5. All the results presented till then are obtained using systems with fixed numbers of NPs:  $N_1 = 10,000$  and  $N_2 = 200$ , which yield an overall particle area density of  $\rho \approx 0.08$  and an area fraction of  $\phi_2 \approx 1/4$  for the large species. Aggregate structures assembled from a single species of NPs at similar particle area density are shown in Fig. S2 for comparison. Like unary assembly of NPs, the binary system of NPs also formed ramified fractal network structures regardless of the sticking probabilities, as shown in Fig. 1. Based on how NP2 is incorporated into the network, we classified the structures into three phases: “integrated”, “covered”, and “leaved” phases. The corresponding morphological phase diagram as a function of the three sticking probabilities is shown in Fig. 1a, and representative structures from the three phase labelled I1, I2, C, L1, and L2 are provided in Fig. 1b–f.

In the “integrated” phase, both NP species are well-integrated into the fractal network, with NP2 particles remaining either isolated (Fig. 1b) or aggregated (Fig. 1c). This phase is obtained when the small particles (NP1) bind to each other at similar rates as they do to the large particles (NP2). When both these rates are large, as in the case of  $p_{11} = 0.4$ ,  $p_{12} = 0.4$ , and  $p_{22} = 0.01$  (yielding structure I1, Fig. 1b), the initial clusters formed are a mixture of homogeneous clusters composed of NP1 particles and heterogeneous clusters containing mostly NP1 particles and few  $[\emptyset(1)]$  isolated NP2 particles, consistent with their small number fraction of 2%. These clusters continue to diffuse, collide, and grow over time to yield a network structure with well dispersed NP2. Simulation snapshots of these various intermediate stages of assembly are provided in Figs. S3 and S4. In contrast, when the rates of NP1 binding to each other and to NP2 are small, as in the case of  $p_{11} = 0.0001$ ,  $p_{12} = 0.0001$ , and  $p_{22} = 0.01$  (I2, Fig. 1c), it allows the NP2 particles to assemble first and form homogeneous

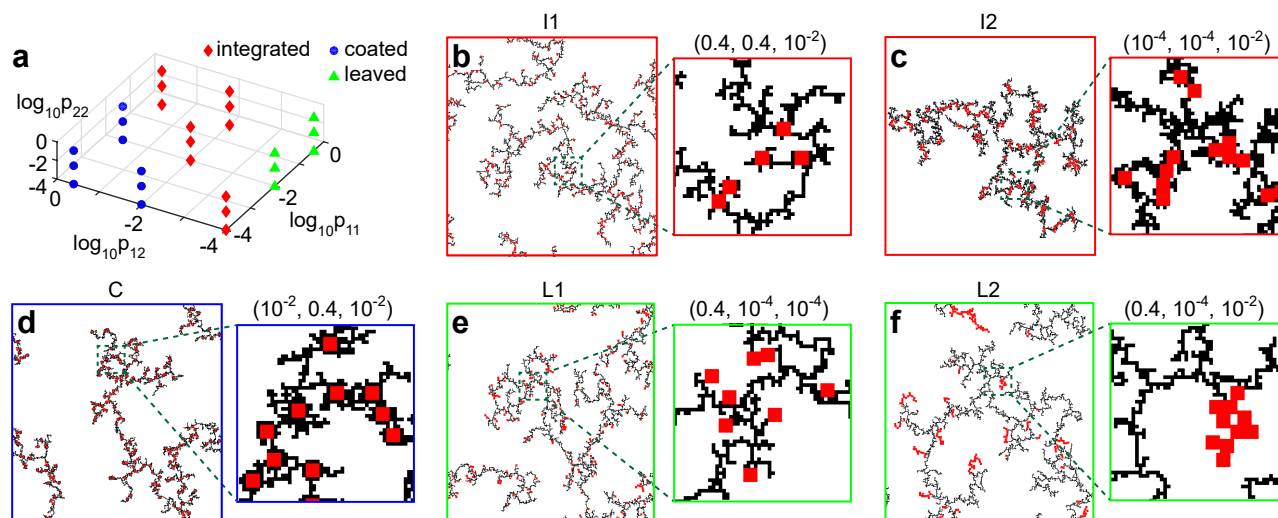


**Fig. 1** Morphology phase diagram and representative structures of different morphologies obtained from simulations. (a) Phase diagram of integrated, coated, and leaved morphologies as a function of intra- and inter-species sticking probabilities. (b–f) Representative structures of an integrated phase with large NPs dispersed (b), integrated phase with large NPs aggregated (c), coated phase (d), leaved phase with large NPs dispersed (e), and leaved phase with large NPs aggregated (f). These five representative structures are denoted by I1, I2, C, L1, and L2, with the associated sticking probabilities specified as  $(p_{11}, p_{12}, p_{22})$ . Small NPs are shown in black and large NPs in red, and the number of NPs are fixed at  $N_1 = 10,000$  and  $N_2 = 200$ .

clusters (Figs. S5 and S6). Only after these clusters are unable to grow further due to their large size and vanishing diffusivities do the NP1 particles start to form clusters of their own by sticking to each other, sometimes using the NP2 aggregates as seeds. Further assembly of these pure and NP2-seeded clusters leads to the integrated phase containing aggregates of large NPs.

In the “coated” phase, the NP2 particles are fully coated with NP1 particles and well dispersed within the NP1 network (Fig. 1d). This phase is observed when the affinity between NPs of different species is much greater than that between particles of the same species, causing NP1-NP2 binding events to occur at much faster rates than NP1-NP1 and NP2-NP2 binding events. Figures S7 and S8, which depict the intermediate stages of assembly for the representative structure obtained with  $p_{11} = 0.01$ ,  $p_{12} = 0.4$ , and  $p_{22} = 0.01$  (C, Fig. 1d), illustrate how NP1 rapidly coats the surface of NP2 and how the remaining NP1 particles continue to assemble into larger clusters by the sticking to themselves and to the NP1 particles coating NP2 particles, ultimately forming the network structure C shown in Fig. 1d. We find that >80% of the neighboring sites of NP2 are occupied by NP1 particles in this phase, unlike the integrated phase where the surface coverages range between 20% and 60%.

Lastly, the “leaved” phase is observed when the affinity between NP1 particles is much stronger than that between NP1 and NP2 particles, and accordingly NP1-NP1 binding occurs at much faster rate than NP1-NP2 binding. In this phase, NP1 particles assemble and form a network first, and then individual or clusters of NP2 particles collide with the NP1 network and attach to it like “leaves” attached to the branches of a tree (Fig. 1e and Fig. 1f). When  $p_{11} = 0.4$  and  $p_{12} = 0.0001$ , and  $p_{22} = 0.0001$  is *small*, NP2 adheres as individual particles to the network, as a result of slow NP2-NP2 binding rates, to form a network with

“small” leaves (L1, Fig. 1e). On the other hand, when  $p_{11} = 0.4$  and  $p_{12} = 0.0001$ , but  $p_{22} = 0.01$  is *large*, the NP2 particles are able to form clusters of their own before attaching to the network, leading to a network with “big” leaves (L2, Fig. 1f). The intermediate stages of assembly leading to both kinds of networks (with small and big leaves) are provided in Figs. S9–S12.

Our results demonstrate how the relative time scales or rates of binding events between the two species of NPs govern the resulting morphology of the NP aggregates and how this morphology can be tuned via the sticking probabilities between particles, in other words, the energy barriers in interparticle interactions. The apparent insensitivity of the phase diagram shown in Fig. 1a to the magnitude of  $p_{22}$  is related partly to the small proportion of NP2 particles in the system, causing binding interactions mediated by NP1 to take precedence over those mediated by NP2, and partly to our definition of phases, where isolated and aggregated forms of NP2 particles in the integrated and leaved phases are classified as sub-phases and not independent phases.

### 3.2 Local composition and arrangement

We next analyzed the local composition and spatial distribution of NPs in the obtained aggregates, properties expected to be important for applications that rely on coupling between neighboring particles. For instance, plasmonic resonances exhibited by assemblies of noble metal NPs are sensitive to not only interparticle distances and orientations but also the type and coordination number of interparticle contacts.<sup>7,39,46</sup> Similarly, the presence of interparticle heterojunctions can provide dramatically improved catalytic activity when the different particle species function synergistically with each other.<sup>43,47</sup> The local stoichiometry and arrangement of particles could also be highly relevant to the conduction of charge carriers<sup>48</sup> and the collective optical proper-

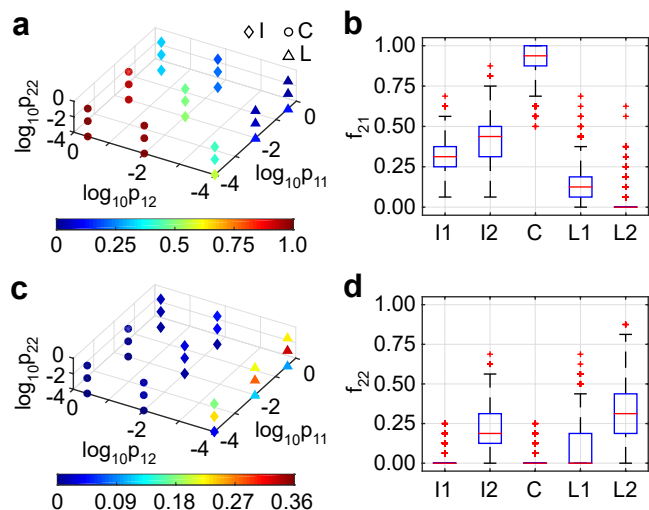


**Fig. 2** Local composition of binary NP aggregates. (a) Average value of  $f_{21}$ , the fraction of neighboring sites of NP2 occupied by NP1, as a function of sticking probabilities. “I”, “C” and “L” in the figure denote integrated, coated and leaved phases. (b) Whisker plot of  $f_{21}$  for the five representative structures shown in Fig. 1. The outliers are plotted individually using the red “+” symbol. (c) Average value of  $f_{22}$ , the fraction of neighboring sites of NP2 occupied by NP2 as a function of sticking probabilities. (d) Whisker plot of  $f_{22}$  for the same representative structures.

ties<sup>49</sup> of polymer nanocomposites.

The local composition of our NP aggregates was characterized in terms of the fraction of neighboring sites of NP2 particles that are occupied by NP1 (Fig. 2a; also see Fig. S13) and NP2 (Fig. 2c; also see Fig. S14), which are denoted by  $f_{21}$  and  $f_{22}$ . In the integrated phase, the NP1-NP2 and NP1-NP1 binding events occur at similar time scales, so a moderate number of NP1 particles adhere to the surface of NP2 particles, and the remaining NP1 particles stick to each other and form clusters. Consequently  $f_{21}$  is in the intermediate range of 20%-50% (Fig. 2a and Fig. 2b). The magnitude of  $f_{22}$  depends on the rate of NP2-NP2 binding relative to the other two binding events, and its value is close to zero when the rate is small (I1, Fig. 2c) and reaches 15% to 25% when the rate is comparable or larger (I2, Fig. 2d). In the coated phase, NP1-NP2 binding events occur at a fast rate, and accordingly NP1 particles have sufficient time to cover the entire surfaces of NP2 before they successfully stick to each other. As a result,  $f_{21}$  is close to 1 and  $f_{22}$  is close to 0 (Fig. 2b and Fig. 2d). In the leaved phase, NP1 particles form a network first before NP2 particles attach individually or in a clustered state to the network. Hence, only a few NP1 particles contact NP2 particles, with  $f_{21}$  less than 20% (Fig. 2b). Depending on whether NP2 attach individually or as aggregates,  $f_{22}$  can be close to zero (L1, Fig. 2d) or reach 20%-35% (L2, Fig. 2d). These results show that the binding kinetics of NPs within and across species dictates not only the overall morphology of the aggregates but also their local environment.

The spatial distribution of NPs was characterized in terms of the radial distribution functions (RDFs)  $g(r)$  between NPs, which

was calculated as follows for like and unlike pairs of NPs:

$$g_{\alpha\alpha}(r) = \frac{1}{\pi r \eta_{\alpha} N_{\alpha}} \sum_{i=1}^{N_{\alpha}-1} \sum_{j>i}^{N_{\alpha}} \langle \delta(|r_{ij} - r|) \rangle, \quad (2)$$

$$g_{12}(r) = \frac{1}{2\pi r \eta_1 \eta_2 N_1} \sum_{i=1}^{N_1} \sum_{j=1}^{N_2} \langle \delta(|r_{ij} - r|) \rangle, \quad (3)$$

where  $\alpha = 1$  and  $2$  denotes NP1 and NP2,  $N_1$  and  $N_2$  are the number of NPs of the two species,  $\eta_1$  and  $\eta_2$  are their number densities (number of particles per unit area),  $r_{ij}$  is the distance between NP  $i$  and  $j$ , and  $\delta$  is the Dirac delta function.

Figure 3 presents the computed RDFs  $g_{11}$ ,  $g_{12}$ , and  $g_{22}$  for all identified phases. Note that due to the NPs being restricted to lattice sites, the RDFs are discontinuous and exhibit discrete peaks. Examining first the RDF between NP1 particles, we find that all phases yield more or less similar  $g_{11}$ , with all RDFs exhibiting peaks at similar interparticle distances albeit with slightly different heights. In particular, the peaks at short distances, e.g., the first four peaks, corresponding to the first-, second-, and third-nearest neighbors, are slightly higher in the integrated phase with aggregated NP2 particles (I2, Fig. 3b) as compared to the rest of the phases, including the integrated phase with isolated NP2 particles (I1, Fig. 3a; also see Fig. S15). The reason is that the sticking probability  $p_{11}$  between NP1 particles is much smaller in I2 as compared to the other phases (e.g.,  $p_{11} = 10^{-4}$  in I2 vs 0.01 or 0.4 in other phases). This leads to RLCA-like conditions whereby NP1 particles assemble into denser structures with more NP1 neighbors around NP1 particles, leading NP1 network in I2 having slightly thicker branches than in the other phases (see Fig. 1c).

We next examined the RDF between NP2 particles, which exhibit a larger closest-separation distance of  $r = 4$  due to their larger size. As expected, the integrated and leaved phases in which NP2 particles are present in an aggregated state (I2, Fig. 1c and L2, Fig. 1f) exhibit the largest peaks in  $g_{22}$ , especially at distances between 4 and 5 representing directly contacting particles (Figs. 3b and 3e; also see Figs. S16b and S16e). Even in the leaved phase in which NP2 particles exhibit very slow sticking probability with each other and remain relatively more dispersed (L1, Fig. 1e), we observe appreciable peaks in  $g_{22}$  (Fig. 3d and Fig. S16d). Only in the integrated and coated phase in which NP2 particles get incorporated individually as bare or NP1-coated particles into the growing network of NP1 particles (L1, Fig. 1b and C, Fig. 1d), do these peaks in  $g_{22}$  become truly negligible (Figs. 3a and 3c; Figs. S16a and S16c). Thus, interestingly, the *inter-species* rate of binding between NP1 and NP2 is more important than the *intra-species* binding rate between NP2 in determining the aggregation state of NP2.

Lastly, we examined the RDF between NP1 and NP2 particles. As expected, the coated phase exhibits the most significant peaks in  $g_{12}$  (Fig. 3c; also see Fig. S17c), as more than 90% of the surface of NP2 particles is covered by NP1 particles in this phase, a result of  $p_{12} \gg p_{11}, p_{22}$ . These peaks are less significant but still appreciable in the integrated phase (Fig. 3a and 3b; Figs. S17a

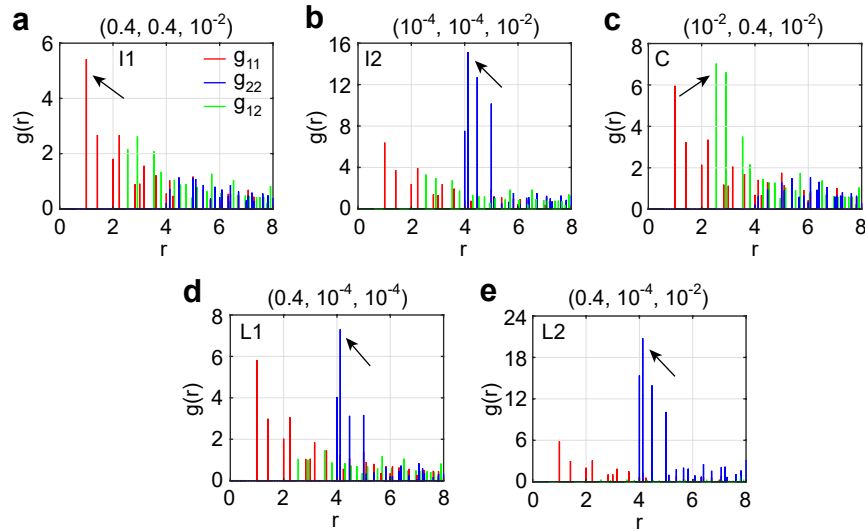


**Fig. 3** NP-NP radial distribution function for the five representative structures shown in Fig. 1. Each figure is labeled with the corresponding structure I1, I2, C, L1, and L2. The arrows show the most prominent peaks in each figure. The number of NPs in the system are fixed at  $N_1 = 10,000$  and  $N_2 = 200$ . The sticking probabilities are specified as  $(p_{11}, p_{12}, p_{22})$ .

and S17b) and almost negligible in the leaved phase (Figs. 3d and 3e; Figs. S17d and S17e).

Overall, the most prominent peaks in the RDFs arise from  $g_{11}$  in the integrated phase with dispersed NPs (I1, Fig. 3a), from  $g_{12}$  in the coated phase (Fig. 3c), and from  $g_{22}$  in the remaining phases (I2, L1 and L2, Figs. 3b, 3d and 3e). Furthermore, among the three RDFs,  $g_{11}$  is clearly the most insensitive to the nature of the phase formed. This is consistent with NP1 particles dominating the overall morphology of the binary aggregates (see Fig. 1), likely due to their higher number density and diffusivities compared to NP2. Our results also indicate that while NP1 always forms branched-network structures, NP2 particles either form compact aggregates or remain dispersed in the system.

### 3.3 Fractal dimension

An important feature of the obtained NP aggregates is their self-similarity over different length scales, which can be described by their fractal dimension  $d_f$ . In the context of polymer nanocomposites, the fractal dimension of the particle aggregates determines to an extent the measured optical scattering and absorption spectra of the composites<sup>50,51</sup> and the particle loadings required to achieve percolation,<sup>18</sup> which is relevant to applications such as mechanical reinforcement.<sup>5,11</sup> Unlike deterministic fractals, our structures are random fractals and do not possess a specific repeating structural motif. There are several methods to calculate the fractal dimension of random fractals.<sup>52</sup> One method is through the relationship between the cumulative distribution function  $C(r)$  and the radius  $r$ :<sup>30</sup>

$$C(r) \sim (r)^{d_f-d}, \quad (4)$$

where  $C(r)$  is the fraction of lattice sites occupied by NPs in a circle of radius  $r$  centered at any point within the NP cluster, and  $d$  is the system dimensions ( $d = 2$ ). Another method is through

the relationship between cluster mass  $M$  (cluster size  $s$ ) and its radius of gyration  $R_g$ :

$$M \sim (R_g)^{d_f}. \quad (5)$$

A third method is through the structure factor  $S(q)$ , which can be calculated as:<sup>53,54</sup>

$$S(q) = N^{-1} \sum_{i,j=1}^N \frac{\sin(qr_{ij})}{qr_{ij}}, \quad (6)$$

where  $q$  is the magnitude of the scattering wave vector,  $N$  is the cluster size (total number of lattice sites occupied by the cluster), and  $r_{ij}$  is the distance between NP  $i$  and NP  $j$ . At intermediate values of  $q$ , i.e.,  $1/R_g < q < 1/s_0$ ,  $S(q)$  exhibits the power-law behavior  $\sim q^{-d_f}$ .

In this work, we used all three methods to calculate  $d_f$ . Figure 4a presents a typical  $C(r)$  function (calculated for the I1 structure presented in Fig. 1b) showing how it decays with  $r$ , and how  $d_f$  can be estimated from the sum of its slope (in a log-log plot) and  $d$ . Figure 4b shows the scaling of  $M$  with  $R_g$  for the same structure, and how  $d_f$  can be obtained from its slope in a log-log plot. Lastly, Fig. 4c shows the structure factor (also see Fig. S18), also for the same structure, which allows us to estimate  $d_f$  from the slope of the  $S(q)$  in a log-log plot. The values of  $d_f$  obtained by using the three methods (1.51, 1.54, and 1.51) are quite close. Note that due to the random nature of the aggregates, the methods are not expected to yield identical fractal dimensions.

The fractal dimensions of aggregates obtained for the various combinations of sticking probabilities explored thus far and calculated using these three methods are presented in Figs. 4d-f. Even though the  $d_f$  values exhibit minor differences between the three methods, the general trend we obtain is that  $d_f$  is small when  $p_{11}$  and  $p_{12}$  are relatively large. The reason is that the rate of successful NP1-NP1 and NP1-NP2 binding events is generally higher than that of NP2-NP2 binding events due to the small diffusivity

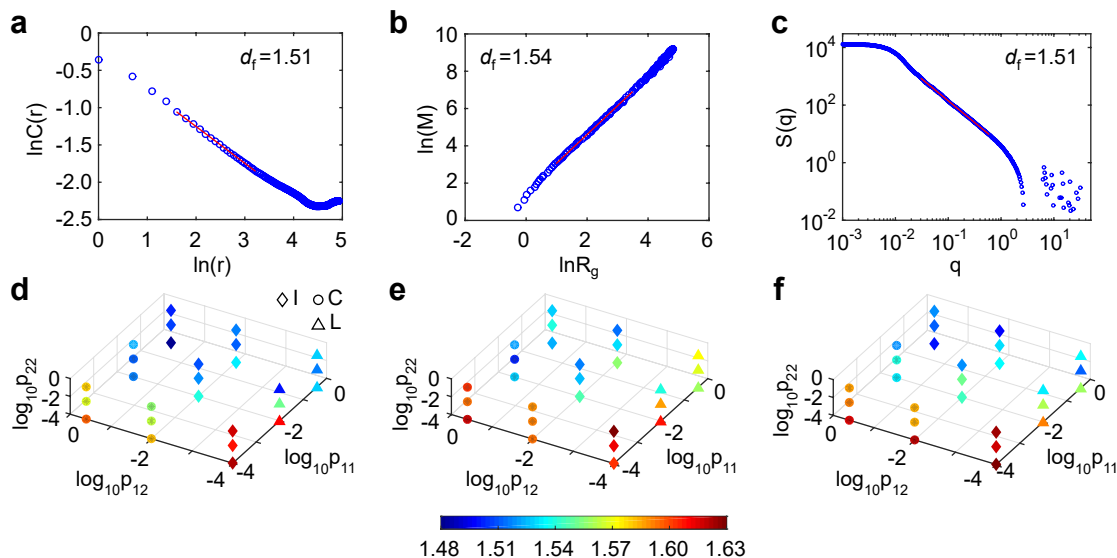


**Fig. 4** Fractal dimension of aggregates. (a–c) Calculation of the fractal dimension  $d_f$  for the representative I1 structure shown in Fig. 1b (with  $p_{11} = 0.4$ ,  $p_{12} = 0.4$ , and  $p_{22} = 0.01$ ) using 3 different methods involving computation of cumulative correlation function  $C(r)$  (a), cluster mass  $M$  (b), and structure factor  $S(q)$  (c). (d–f) Fractal dimension of aggregates obtained as a function of sticking probabilities using the three methods involving computation of  $C(r)$  (d),  $M$  (e), and  $S(q)$  (f). “I”, “C” and “L” in the figure denote integrated, coated and leaved phases.

and low concentration of NP2 particles, and hence the aggregation process is dominated by NP1-NP1 and NP1-NP2 bindings. Consequently, their sticking probabilities  $p_{11}$  and  $p_{12}$  determine whether the assembly process is diffusion limited, which leads to low  $d_f$ , or reaction limited, which leads to higher  $d_f$ .

### 3.4 Porosity and aggregate size

Another useful property to characterize, especially for the network-like structures obtained here, is their porosity, a property that is highly relevant to applications in gas separation, filtration, sensing, and catalysis.<sup>15,16,55</sup> To obtain the pore size distribution and overall compactness of our aggregates, we employed the following scheme (Fig. 5a): We first retrieved the unwrapped coordinates of the aggregate. Second, we obtained the smallest possible ellipse that encapsulates roughly 60% of the NPs; the area  $\pi R_1 R_2$  of the ellipse, where  $R_1$  and  $R_2$  are its semi-major and semi-minor axes, provides a measure of the size of the aggregate and its compactness. Next, we sampled the pores within the aggregate, using the ellipse as a boundary. To this end, we randomly picked an unoccupied lattice site within the ellipse and used that point as the origin of a circle whose size was expanded until it began to contact the aggregate. If the circle exhibited one contact point with the aggregate, the circle was translated along the line connecting the origin and the contact point and expanded in an iterative manner until the circle started to contact another point on the aggregate. Such a circle with two contact points was translated along the perpendicular bisector of the line connecting the two contact points and expanded in an iterative manner until the circle contacted a third point on the aggregate. If the three contact points formed an acute triangle, then the circle was completely confined by the NPs of the aggregate. If the three points formed an obtuse triangle, then the circle was further

translated and expanded until it was completely confined by the aggregate. The diameter  $d_p$  of the confined circle then gives the pore size of the aggregate at the initially chosen lattice site. Sampling  $d_p$  across multiple (100,000 times for each aggregate) such randomly-picked unoccupied sites within the ellipse yielded the area-weighted pore-size distribution, which can be appropriately averaged to obtain the number- and area-averaged pore size. See ESI for more details.

Figure 5b–d shows the aggregate size and their number- and area-averaged pore sizes for the 27 systems investigated here with distinct combinations of sticking probabilities. To improve accuracy, all results were averaged over 15 independent simulation runs at each condition. Our results indicate that the size of the aggregates is determined primarily by the magnitude of  $p_{11}$ , with large sticking probabilities leading to large aggregates, and  $p_{12}$  and  $p_{22}$  play a negligible role (Fig. 5b). As the total number of particles is held constant, a large aggregate also means a more extended structure, and a small aggregate means a more compact structure. These results are consistent with NP1-NP1 assembly driving the overall morphology of the aggregates and with the aggregates becoming increasingly tenuous and extended with increasing sticking propensities, as discussed earlier. We find that variations in  $p_{11}$  can cause up to two-fold variations in the compaction or extension of the aggregates. The relationship between average pore size and  $p_{11}$  is also very clear: reducing  $p_{11}$  results in structures with smaller pore size (Fig. 5c and Fig. 5d), although this trend is less evident for the area-averaged pore size than the number-averaged pore size. Interestingly, we observe a large, almost five-fold, difference in the values of the area- and number-averaged pore sizes. This difference clearly arises due to the large polydispersity in pore sizes, testament to the random and fractal nature of the structures. Overall, our results indicate

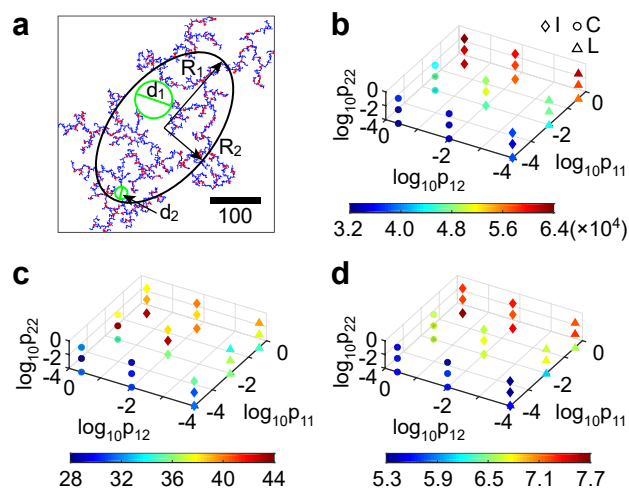


**Fig. 5** Cluster size and pore size of the aggregates. (a) Unwrapped structure of an aggregate obtained using  $p_{11} = 0.4$ ,  $p_{12} = 0.4$ , and  $p_{22} = 0.01$ . The black ellipse is the smallest ellipse enclosing 60% of the NPs in the aggregate.  $R_1$  and  $R_2$  are the semi-major and semi-minor axes of the ellipse. The two circles of diameter  $d_1$  and  $d_2$  depict two representative pores in the structure. The scale bar corresponds to a length of 100 lattice sites. (b) Size of aggregates, as given by the area of the ellipse, as a function of sticking probabilities. The number of NPs are fixed at  $N_1 = 10,000$  and  $N_2 = 200$ . “I”, “C” and “L” in the figure denote integrated, coated and leaved phases. (c–d) Area-average (c) and number-average (d) pore size of the aggregates as a function of sticking probabilities.

that the cluster size and porosity of the aggregates can be tuned by changing the affinity between the NPs, especially the dominant species.

### 3.5 Effects of NP stoichiometry, loading, and system size

All results presented so far were obtained using systems containing  $N_1 = 10,000$  and  $N_2 = 200$  particles, corresponding to NP2 area fraction of  $\phi_2 = 0.24$  and an overall particle density of  $\rho = 0.083$ . We also investigated 8 additional systems with  $N_1 = 10,000$ , 20,000, or 30,000 and  $N_2 = 200$ , 400, or 800, spanning a broad range of area fractions ( $\phi_2 = 0.10$ – $0.56$ ) and overall densities ( $\rho = 0.083$ – $0.27$ ) to study the effects of these two parameters. We characterized the morphologies of the aggregate structures obtained from these additional systems, and also computed the local composition, fractal dimension, size, and porosity of the aggregates for one of the additional systems, the one with high NP loading of  $N_1 = 30,000$  and  $N_2 = 800$ . While complete phase diagrams in morphologies and properties along with representative structures for these new systems are provided in Figs. S19–S29 in the ESI, below we highlight only the most salient aspects of these results.

We found that systems with mass fractions  $\phi_2 \lesssim 0.25$ , irrespective of the overall particle loadings, yielded phase diagrams with integrated, coated, and leaved morphologies very similar to those presented in Fig. 1. This includes systems with  $[N_1 \ N_2] = [20,000 \ 200]$  (Fig. S21),  $[20,000 \ 400]$  (Fig. S22),  $[30,000 \ 200]$  (Fig. S24), and  $[30,000 \ 400]$  (Fig. S25).

The rest of the systems with  $[N_1 \ N_2] = [10,000 \ 400]$  (Fig. S19),

$[10,000 \ 800]$  (Fig. S20),  $[20,000 \ 800]$  (Fig. S23), and  $[30,000 \ 800]$  (Fig. S26) in which NP2 particles are present at higher mass fraction exhibited a new morphology (in addition to the integrated, coated and leaved phases) that we refer to as the “blocked” phase. Figure 6 illustrates various properties of this phase using the example of a system containing  $N_1 = 10,000$  and  $N_2 = 800$  at  $\phi_2 \approx 0.56$ . In the blocked phase, the two species of NPs are well segregated, as in the leaved phase with aggregated NP2 particles (L2; Fig. 1f), except that the NP2 leaves are long enough to bridge distinct portions of the NP1 network, resulting in a contiguous network of long branches or blocks of NP1 and NP2 particles (Fig. 6b; Figs. S19f, S20f, S23f, and S26f). The phase diagram presented in Fig. 6a reveals that the blocked phase appears when NP1 particles stick to each other at much higher rates than they do to NP2 particles, again, conditions similar to those producing the leaved phase at smaller NP2 fractions. Here, though, the NP2 particles are available at high concentration, which allows the particles to assemble into large clusters while the NP1 particles are still in the process of forming the network. This provides these large NP2 clusters the time to integrate with the NP1 clusters before they all come together to form a closed network. However, if the sticking probability  $p_{22}$  between NP2 particles is very small, they assemble too slowly and are unable to properly integrate with the network, and the usual leaved phase ensues (green triangle in Fig. 6a). Since NP1 and NP2 particles are segregated from each other, the RDF peaks in both  $g_{11}$  and  $g_{22}$  are strong while those in  $g_{12}$  remain quite weak (Fig. 6c). The fractal dimension of the structure is about 1.54, as calculated from its structure factor (Fig. 6d), which is quite similar to that of the integrated phase.

Apart from the new phase, the phase diagram in Fig. 6a shows another difference, albeit subtle, from that of Fig. 1a. Specifically, all systems with  $p_{11} = 0.01$ ,  $p_{12} = 0.4$  that formed a coated phase at low  $\phi_2$  now form an integrated phase at high  $\phi_2$ . The reason is the number of NP1 particles are not sufficient to completely coat the surface of NP2 particles. As a result, the final structure with relatively bare NP2 particles integrated within the NP1 network resemble more the integrated phase than a coated phase, see Fig. S27 for the structure.

We next compared the local compositions, fractal dimensions, cluster sizes, and porosities discussed thus far for the system at low particle loading (Figs. 2, 4, and 5) against those computed for one of the additional systems in the opposite regime of high loading (Fig. S28). Our comparison revealed that many of the already discussed trends in these properties with respect to the sticking probabilities are also observed at high loading, though some intriguing differences also arise. In particular, we found that the computed  $f_{21}$  and  $f_{22}$  remain similar across the two systems (Fig. 2a and 2b vs. Fig. S28a and S28b), suggesting that the local composition of aggregates is *not* affected by NP loading. The cluster size also decreases with decreasing  $p_{11}$  in both systems (Fig. 5b vs. Fig. S28c), though the *relative* size variation with  $p_{11}$  is much smaller at high loading. Interestingly, we found that the pore size becomes larger with increasing  $p_{11}$  at high load-

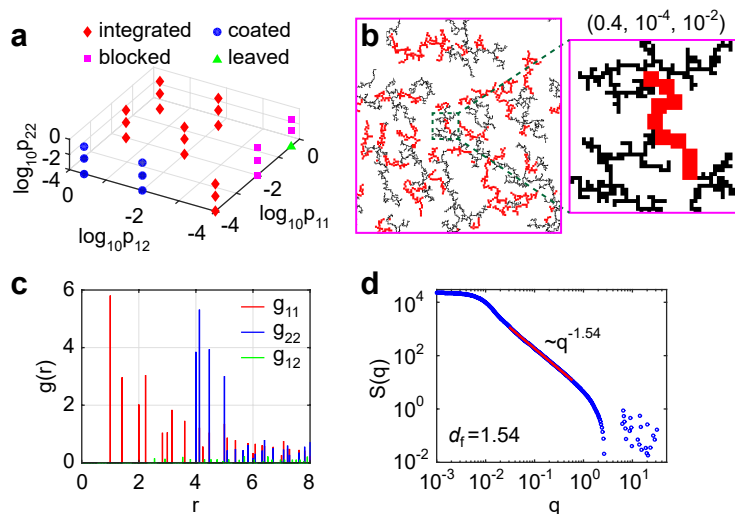


**Fig. 6** Structural characteristics of the blocked phase. (a) Morphology of the blocked phase. The sticking probabilities are marked in the figures as  $(p_{11}, p_{12}, p_{22})$ . The number of NPs in the system is  $N_1=10000$  and  $N_2=800$ . (c) Radial distribution functions between NPs for the structure shown in (b). (d) Structure factor of the structure shown in (b), and the fractal dimension  $d_f$  obtained from it.

ings (Fig. S28d), a trend opposite to that observed at low loadings (Fig. 5c). This difference may be understood as: at low loading, increasing  $p_{11}$  leads to larger and sparser clusters, which naturally then leads to larger pores. However, at high loading, the cluster sizes are comparable at small and large  $p_{11}$ , but decreasing  $p_{11}$  leads to thicker network branches and thereby larger pore (see Fig. S29). This observation also likely explains why the fractal dimension was found to increase with increasing  $p_{11}$  at high loading (Fig. S28e), but decrease with the same sticking probability at low loadings (Fig. 4f).

We also found that the fractal networks become increasingly compact with smaller pores and higher percolation as the overall density is increased, keeping the mass fraction of the two species more or less constant. Comparing for instance the structures obtained with  $[N_1 N_2] = [10,000 200]$  at  $\rho = 0.083$  (Fig. 1),  $[N_1 N_2] = [20,000 400]$  at  $\rho = 0.17$  (Fig. S22), and  $[N_1 N_2] = [30,000 400]$  at  $\rho = 0.23$  (Fig. S25) in the case of  $p_{11} = 0.4$ ,  $p_{12} = 0.4$ , and  $p_{22} = 0.01$ , we found the area-average pore size decreases from 39 to 23 to 12 while the fractal dimension only changes little between 1.53 and 1.57.

Lastly, to confirm that all intensive properties of aggregates reported so far are insensitive to our choice of system size, we performed simulations using a  $4\times$  larger simulation box ( $800 \times 800$  lattice with  $N_1 = 40000, N_2 = 800, p_{11} = p_{12} = p_{22} = 0.4$ ) corresponding to one of the studied systems (with  $N_1 = 10000, N_2 = 200, p_{11} = p_{12} = p_{22} = 0.4$ ). Our results show that the local distribution of NPs and the fractal dimension of the aggregates are indeed unaffected by system size (Fig. S30 and Fig. S31), whereas the overall size of aggregates and their average pore size shift towards larger values as the clusters grow into larger aggregates on the larger lattice and larger pores begin to appear (compare Figs. S30a and S30b). Although the absolute values of the pore sizes may change, the relative variation in pore sizes as a function of sticking probabilities, NP densities and stoichiometries is

not expected to change with box size.

## 4 Discussion

We used lattice Monte Carlo simulations to explore the possible kinetically-trapped aggregate morphologies obtained from co-assembly of a binary system of NPs in two dimensions. This work is motivated by the observation that the random aggregates typically obtained from homogeneous systems of particles exhibit a limited set of morphologies. Therefore, we sought to examine if the addition of a second species of particles of different size, diffusivity, and binding propensity could increase the diversity of morphologies achievable through random aggregation. We hypothesized that the new species would introduce additional length and time scales related to the size of the new species and its rates of assembly with itself and with the existing species. Our simulations show that, indeed, the random fractal networks formed from binary mixtures of small and large NPs exhibit much larger variations in morphology compared to those formed from a single NP species. In particular, based on the relative concentration of the two species and the magnitudes of intra- and inter-species sticking probabilities, the NPs were found to assemble into one of the four distinct morphologies that we termed integrated, coated, leaved, and blocked phases. These morphologies differed most significantly from each other in: (1) local distribution of small NPs around the large NPs, with the fraction of surface area of large NPs occupied by small NPs varying from 3% to 98% across the various morphologies; and (2) spatial organization of large NPs within the networks, where the large NPs were present in either dispersed or aggregated form and either segregated or fully integrated into the small-NP structures. The fractal networks assembled from binary systems also exhibit much larger variations in pore sizes compared to those assembled from a single species at equivalent particle area densities (28–44 from two species vs. 32–36 from one species; Fig. 7c; also see Table S1), though the

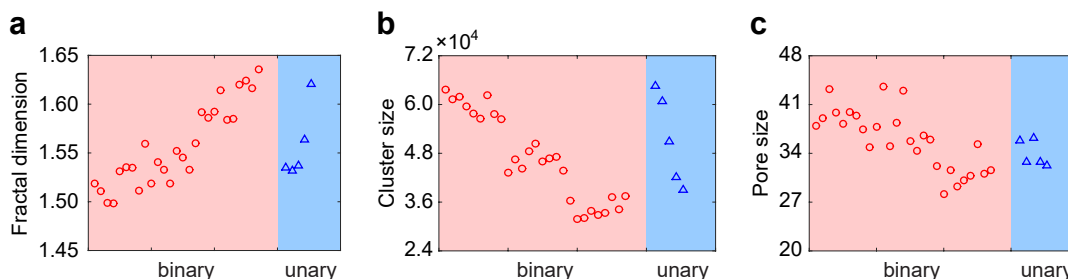


**Fig. 7** Comparison of the fractal dimension (a), cluster size (b) and pore size (c) of aggregate structures obtained from binary and unary NP systems. Red circles and blue triangles show property values obtained from binary and unary systems, respectively. For binary assembly, the number of NPs in the system are fixed at  $N_1=10\,000$  and  $N_2=200$ , and the sticking probabilities are varied from  $10^{-4}$  to 0.4. For unary assembly involving only small NPs, the number of such NPs is fixed at 13 200, and the sticking probabilities are varied from  $10^{-4}$  to 0.4 ( $10^{-4}$ ,  $10^{-3}$ ,  $10^{-2}$ , 0.1, 0.4). Fractal dimensions were calculated from structure factors.

corresponding increases in the range of achievable fractal dimensions (1.50–1.64 vs. 1.53–1.62; Fig. 7a) and cluster sizes (32000–64000 vs. 39000–64000; Fig. 7b) are more modest.

Our results demonstrate how the morphology of binary aggregates of NPs can be effectively tuned by varying the relative rates of the three binding events underlying assembly, i.e., NP1-NP1, NP2-NP2, and NP1-NP2 binding. One can estimate these rates at the early stages of assembly when only isolated particles exist. Based on reaction-rate theory,<sup>56</sup> the rate of NP1-NP2 binding events in 2D is given by  $R_{12} \simeq 2\pi(D_1 + D_2)\eta_1\eta_2p_{12}f(s_1, s_2)$ , where  $\eta_1$  and  $\eta_2$  are the concentrations (number densities) of the two species,  $D_1$  and  $D_2$  are their self-diffusivities, and  $f(s_1, s_2)$  is a logarithmically increasing function of their sizes. Similarly, the rates of NP1-NP1 and NP2-NP2 binding events are given by  $R_{11} \simeq 4\pi D_1 \eta_1^2 p_{11} f(s_1)$  and  $R_{22} \simeq 4\pi D_2 \eta_2^2 p_{22} f(s_2)$ . Given that diffusivity and particle size have opposite effects on the rate, and in fact almost cancel out in 3D, the NP binding rates then mostly depend on the concentrations and the sticking probabilities of the binding partners. While both effects similarly modulate the binding rates (both proportionally), the sticking probabilities enable the widest possible modulation in binding rates. The reason is that one can achieve orders of magnitude variations in binding rates through moderate changes in the interaction energy barriers between particle due to exponential dependence of sticking probabilities on energy barriers. Indeed, the largest variations in network morphologies obtained in this work were achieved by orders of magnitude variations in the three sticking probabilities, and the effects of stoichiometry, which only varied four-fold, were understandably more subtle.

The NP networks predicted here could be especially relevant in polymer nanocomposites, where fractal networks have been shown to significantly enhance the mechanical properties of polymers,<sup>5,11</sup> improve the ionic conductivity of solid polymer electrolytes,<sup>12,13,57–59</sup> and enable other applications in optical data storage, sensing, imaging, catalysis, gas-liquid barriers, and photothermal therapy<sup>16,60–63</sup>, where porous networks of NPs are required. The new network morphologies obtained could enable further improvements in such functions. For instance, the modulus and yield stress of polypropylene were found to be most

strongly enhanced when both nanoclay and  $\text{CaCO}_3$  NPs were incorporated into the polymer as opposed to individual species of NPs at similar volume fractions.<sup>64</sup> Furthermore, the existence of two species of NPs within the networks coupled with the ability to tune the number of contacts and overall organization of the two species of NPs within the networks could impart new functions into composites not possible with single species of NPs. For instance, interfaces between two types of NPs are highly relevant to heterogeneous catalysis,<sup>15,43</sup> electron tunnelling,<sup>65</sup> charge separation,<sup>66</sup> and plasmonics.<sup>7,39,46,67</sup>

While this study focused on a 2D assembly system, the aggregate morphologies and trends in properties presented here should remain qualitatively similar to those expected from 3D systems. Given that the underlying physics governing assembly morphology remains the same across 2D and 3D systems (i.e., large NPs diffusing slower than small NPs but providing a larger contact area for collision and sticking, particle stoichiometry governing frequencies of intra- vs. inter-species collisions, and sticking probabilities governing reaction- vs. diffusion-limited regimes of assembly), we expect the same integrated, coated, leaved, and blocked phases to also appear in 3D. In the same vein, we also expect to observe similar trends in the relationship between the local distribution, fractal dimensions, and porosities of the aggregated structures with the input sticking probabilities, even though the absolute values of some of these properties will likely be different in 3D. Thus, while it is necessary to extend the assembly of binary NPs to 3D systems, the results obtained here from the 2D model already provides useful insights and guidelines for understanding assembly of binary networks in 3D.

## 5 Conclusions

We investigated via lattice simulations the range of network morphologies achievable through kinetic assembly of binary systems of NPs. We showed how the sizes, stoichiometries, and affinities between NPs could be exploited to regulate the kinetics of intra- and inter-species binding events and create a range of heterogeneous network morphologies, which could be categorized into four main classes—integrated, coated, leaved, and blocked phases. These phases exhibited striking differences in the local composition and spatial distribution of NPs as well fractal dimen-

sions and porosities. These new heterogeneous particle networks have the potential to introduce novel properties into polymer-NP composites, or improve existing properties of composites, especially in the context of mechanical, electrical, and optical composite materials. From a more general point of view, our study also provides fundamental insights into the assembly kinetics of multicomponent particle systems.

## Conflicts of interest

There are no conflicts to declare.

## Acknowledgements

We thank National Science Foundation (NSF) CMMI Award 1636356 for partial support of this research. Computational resources were provided by NSF's Extreme Science and Engineering Discovery Environment (XSEDE) Program ACI-1053575 and the Duke Computer Cluster. We thank Dr. Andrea Tao and Dr. Benjamin Wiley for useful discussions.

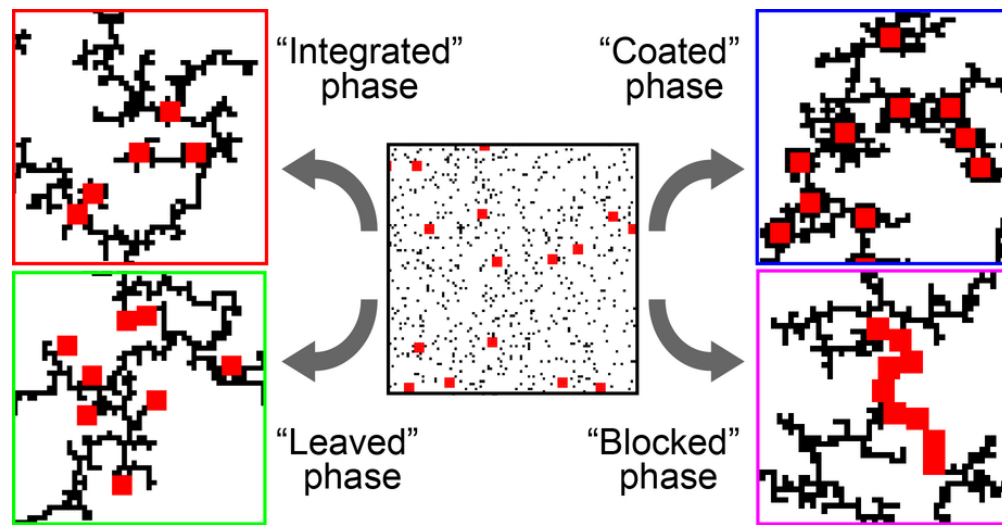
## Notes and references

- 1 A. C. Balazs, T. Emrick and T. P. Russell, *Science*, 2006, **314**, 1107–1110.
- 2 S.-W. Hsu, A. L. Rodarte, M. Som, G. Arya and A. R. Tao, *Chem. Rev.*, 2018, **118**, 3100–3120.
- 3 D. Maillard, S. K. Kumar, B. Fragneaud, J. W. Kysar, A. Rungta, B. C. Benicewicz, H. Deng, L. C. Brinson and J. F. Douglas, *Nano Lett.*, 2012, **12**, 3909–3914.
- 4 S. Y. Fu, X. Q. Feng, B. Lauke and Y. W. Mai, *Compos. Pt. B-Eng.*, 2008, **39**, 933–961.
- 5 P. Akcora, H. Liu, S. K. Kumar, J. Moll, Y. Li, B. C. Benicewicz, L. S. Schadler, D. Acehan, A. Z. Panagiotopoulos, V. Pryamitsyn, V. Ganesan, J. Ilavsky, P. Thiyagarajan, R. H. Colby and J. F. Douglas, *Nat. Mater.*, 2009, **8**, 354–359.
- 6 V. Goel, J. Pietrasik, H. Dong, J. Sharma, K. Matyjaszewski and R. Krishnamoorti, *Macromolecules*, 2011, **44**, 8129–8135.
- 7 B. Gao, G. Arya and A. R. Tao, *Nat. Nanotechnol.*, 2012, **7**, 433–437.
- 8 K. L. Gurunatha, S. Marvi, G. Arya and A. R. Tao, *Nano Lett.*, 2015, **15**, 7377–7382.
- 9 P. J. Lu, E. Zaccarelli, F. Ciulla, A. B. Schofield, F. Sciortino and D. A. Weitz, *Nature*, 2008, **453**, 499–503.
- 10 F. M. Hecht and A. R. Bausch, *Proc. Natl. Acad. Sci. U. S. A.*, 2016, **113**, 8577–8582.
- 11 J. F. Moll, P. Akcora, A. Rungta, S. S. Gong, R. H. Colby, B. C. Benicewicz and S. K. Kumar, *Macromolecules*, 2011, **44**, 7473–7477.
- 12 Z. Zhu, M. Hong, D. Guo, J. Shi, Z. Tao and J. Chen, *J. Am. Chem. Soc.*, 2014, **136**, 16461–16464.
- 13 A. Jarosik, U. Traub, J. Maier and A. Bunde, *Phys. Chem. Chem. Phys.*, 2011, **13**, 2663–2666.
- 14 T. Kashiwagi, F. M. Du, J. F. Douglas, K. I. Winey, R. H. Harris and J. R. Shields, *Nat. Mater.*, 2005, **4**, 928–933.
- 15 H. Song, *Acc. Chem. Res.*, 2015, **48**, 491–499.
- 16 I. Pastoriza-Santos, C. Kinnear, J. Perez-Juste, P. Mulvaney and L. M. Liz-Marzan, *Nat. Rev. Mater.*, 2018, **3**, 375–391.
- 17 M. Y. Lin, H. M. Lindsay, D. A. Weitz, R. C. Ball, R. Klein and P. Meakin, *Nature*, 1989, **339**, 360–362.
- 18 S. Lazzari, L. Nicoud, B. Jaquet, M. Lattuada and M. Morbidelli, *Adv. Colloid Interface Sci.*, 2016, **235**, 1–13.
- 19 C. Xiong and S. Friedlander, *Proc. Natl. Acad. Sci. U.S.A.*, 2001, **98**, 11851–11856.
- 20 R. Mezzenga, P. Schurtenberger, A. Burbidge and M. Michel, *Nat. Mater.*, 2005, **4**, 729.
- 21 Ü. Ö. Köylü, G. Faeth, T. L. Farias and M. d. G. Carvalho, *Combust. Flame*, 1995, **100**, 621–633.
- 22 G. V. R. Born, *Nature*, 1962, **194**, 927–929.
- 23 P. Meakin, *Phys. Rev. Lett.*, 1983, **51**, 1119–1122.
- 24 M. Kolb, R. Botet and R. Jullien, *Phys. Rev. Lett.*, 1983, **51**, 1123–1126.
- 25 C. R. Murthy, B. Gao, A. R. Tao and G. Arya, *Phys. Rev. E: Stat., Nonlinear, Soft Matter Phys.*, 2016, **93**, 022501.
- 26 T. Y. Tang and G. Arya, *Macromolecules*, 2017, **50**, 1167–1183.
- 27 S. F. Tan, S. W. Chee, G. H. Lin and U. Mirsaidov, *Accounts Chem. Res.*, 2017, **50**, 1303–1312.
- 28 K. Zhao and T. G. Mason, *Rep. Prog. Phys.*, 2018, **81**, 126601.
- 29 A. E. Gonzalez, *Phys. Rev. Lett.*, 1993, **71**, 2248–2251.
- 30 C. R. Murthy, B. Gao, A. R. Tao and G. Arya, *Nanoscale*, 2015, **7**, 9793–9805.
- 31 B. Gao, Y. Alvi, V. Li and A. R. Tao, *CrystEngComm*, 2014, **16**, 9434–9440.
- 32 J. Lee, S. J. Lee, K. H. Ahn and S. J. Lee, *Phys. Rev. E: Stat., Nonlinear, Soft Matter Phys.*, 2015, **92**, 012313.
- 33 A. F. Demirörs, J. C. Stiefelwagen, T. Vissers, F. Smalenburg, M. Dijkstra, A. Imhof and A. van Blaaderen, *Phys. Rev. X*, 2015, **5**, 021012.
- 34 F. Pierce, A. Chakrabarti, D. Fry and C. M. Sorensen, *Langmuir*, 2004, **20**, 2498–2502.
- 35 J. Lee, S. J. Lee, K. H. Ah and S. J. Lee, *Langmuir*, 2015, **31**, 13639–13646.
- 36 F. Varrato, L. Di Michele, M. Belushkin, N. Dorsaz, S. H. Nathan, E. Eiser and G. Foffi, *Proc. Natl. Acad. Sci. U. S. A.*, 2012, **109**, 19155–19160.
- 37 L. Di Michele, F. Varrato, J. Kotar, S. H. Nathan, G. Foffi and E. Eiser, *Nat. Commun.*, 2013, **4**, 2007.
- 38 Z. Nie, A. Petukhova and E. Kumacheva, *Nat. Nanotechnol.*, 2010, **5**, 15–25.
- 39 J. A. Fan, C. H. Wu, K. Bao, J. M. Bao, R. Bardhan, N. J. Halas, V. N. Manoharan, P. Nordlander, G. Shvets and F. Capasso, *Science*, 2010, **328**, 1135–1138.
- 40 S. W. Hsu, A. L. Rodarte, M. Som, G. Arya and A. R. Tao, *Chem. Rev.*, 2018, **118**, 3100–3120.
- 41 T.-Y. Tang, Y. Zhou and G. Arya, *ACS Nano*, 2019, **13**, 4111–4123.
- 42 D. A. Weitz, J. S. Huang, M. Y. Lin and J. Sung, *Phys. Rev. Lett.*, 1985, **54**, 1416–1419.

- 43 H. Wu, H. Li, Y. Zhai, X. Xu and Y. Jin, *Adv. Mater.*, 2012, **24**, 1594–1597.
- 44 C. Sorensen, *Aerosol Sci. Technol.*, 2011, **45**, 765–779.
- 45 P. Sandkühler, M. Lattuada, H. Wu, J. Sefcik and M. Morbidelli, *Adv. Colloid Interface Sci.*, 2005, **113**, 65–83.
- 46 T. Tumkur, X. Yang, C. Zhang, J. Yang, Y. Zhang, G. V. Naik, P. Nordlander and N. J. Halas, *Nano Lett.*, 2018, **18**, 2040–2046.
- 47 D. F. Swearer, H. Zhao, L. Zhou, C. Zhang, H. Robotjazi, J. M. P. Martirez, C. M. Krauter, S. Yazdi, M. J. McClain, E. Ringe, E. A. Carter, P. Nordlander and N. J. Halas, *Proceedings of the National Academy of Sciences*, 2016, **113**, 8916–8920.
- 48 S. Sardar, P. Kar, H. Remita, B. Liu, P. Lemmens, S. K. Pal and S. Ghosh, *Sci. Rep.*, 2015, **5**, 17313.
- 49 Y. Jin and S. Dong, *Angew. Chem., Int. Edit.*, 2002, **41**, 1040–1044.
- 50 E. Wolf and O. Toon, *Science*, 2010, **328**, 1266–1268.
- 51 S. Srivastava, M. Haridas and J. Basu, *Bulletin of Materials Science*, 2008, **31**, 213–217.
- 52 G. C. Bushell, Y. D. Yan, D. Woodfield, J. Raper and R. Amal, *Adv. Colloid Interface Sci.*, 2002, **95**, 1–50.
- 53 C. M. Sorensen, *Aerosol Sci. Technol.*, 2001, **35**, 648–687.
- 54 M. Rotterreau, J. C. Gimel, T. Nicolai and D. Durand, *Eur. Phys. J. E*, 2004, **15**, 141–148.
- 55 S. K. Kumar, B. C. Benicewicz, R. A. Vaia and K. I. Winey, *Macromolecules*, 2017, **50**, 714–731.
- 56 S. Chandrasekhar, *Rev. Mod. Phys.*, 1943, **15**, 1.
- 57 S. Srivastava, J. L. Schaefer, Z. C. Yang, Z. Y. Tu and L. A. Archer, *Adv. Mater.*, 2014, **26**, 201–233.
- 58 C. Pfaffhuber, S. Sorgel, K. Weichert, M. Bele, T. Mundinger, M. Gobel and J. Maier, *J. Am. Chem. Soc.*, 2011, **133**, 14514–14517.
- 59 A. J. Bhattacharyya, *J. Phys. Chem. Lett.*, 2012, **3**, 744–750.
- 60 F. Y. Li, J. X. Lu, X. Q. Kong, T. Hyeon and D. S. Ling, *Adv. Mater.*, 2017, **29**, 1605897.
- 61 V. Mulens-Arias, A. Nicolas-Boluda, A. Gehanno, A. Balfourier, F. Carn and F. Gazeau, *Nanoscale*, 2019, **11**, 3344–3359.
- 62 S. Ogasawara and S. Kato, *J. Am. Chem. Soc.*, 2010, **132**, 4608–4613.
- 63 J. Ahn, W. J. Chung, I. Pinnau, J. S. Song, N. Y. Du, G. P. Robertson and M. D. Guiver, *J. Membr. Sci.*, 2010, **346**, 280–287.
- 64 H. B. Chen, M. Z. Wang, Y. Lin, C. M. Chan and J. S. Wu, *J. Appl. Polym. Sci.*, 2007, **106**, 3409–3416.
- 65 H. Qian, S.-W. Hsu, K. Gurunatha, C. T. Riley, J. Zhao, D. Lu, A. R. Tao and Z. Liu, *Nat. Photonics*, 2018, **12**, 485–488.
- 66 Y. Tian and T. Tatsuma, *J. Am. Chem. Soc.*, 2005, **127**, 7632–7637.
- 67 S. Sheikholeslami, Y.-w. Jun, P. K. Jain and A. P. Alivisatos, *Nano Lett.*, 2010, **10**, 2655–2660.

**TOC entry**

Lattice simulations reveal that kinetic assembly of two species of nanoparticles can lead to unique fractal networks with diverse morphologies



TOC figure

77x40mm (300 x 300 DPI)